ConTac: Continuum-Emulated Soft Skinned Arm with Vision-based Shape Sensing and Contact-aware Manipulation

Tuan Tai Nguyen[1], Quan Khanh Luu[1], Dinh Quang Nguyen[2], and Van Anh Ho[1*]

Abstract—Robotic systems employing continuum bodies offer a high degree of dexterity, which provides advantages in terms of accuracy and safety when operating in cluttered environments. However, current methods of describing posture or detecting contact for such continuum structures are focusing on bespoke designs or are limited to a single sensing modality, which could hinder their possibility for scalability and generalization. This study proposes a novel vision-based tactile sensing system, named *ConTac*, that provides both proprioception and tactile detection for a continuum-emulated arm with soft skin. To realize the mentioned functions, we employ two corresponding deep-learning models trained using simulation data. The models are zero-shot applied to real-world data without fine-tuning. The experimental results show that the system could predict the posture of a skinned robot arm with a mean tip position error of 8.83 mm, while the mean error for touch location was 28.86 mm. We then compared the model performance on two different robot modules, proving the justification of the system. An admittance control strategy is then developed using the shape and contact information, allowing the robot arm to react properly to collisions. The proposed method shows potential in adapting to hyper-redundant or continuum robots, enhancing their perception capabilities and control paradigms.

Project website: https://sites.google.com/view/contacsensing

I. INTRODUCTION

Nature has presented us with a wide range of highly dexterous bodies such as an elephant trunk or an octopus tentacle. By adopting the principle of such natural structures into robotic systems, researchers hope to develop continuum robots that offer high robustness and safety [1]–[5]. Owning to having degrees of freedom (DOFs) exceeding the needed DOFs for the performance of a task, continuum robot arms provide great advantages in flexibility, dexterity, and the capability to handle unexpected situations when compared to rigid manipulators. For instance, continuum-body robots' performances are not hindered when reaching a target in cases where obstacles or disturbances are presented [5], [6]. Characterizing the morphology of such highly redundant manipulators remains a major challenge. This is because, during task execution, their bodies tend to form complicated morphologies, especially in cases where the robot is fabricated from soft materials.

[1]Soft Haptics Lab., School of Materials Science, Japan Advanced Institute of Science and Technology, Asahidai 1-1, Nomi, Ishikawa, 923-1292 Japan.
[2]Institute of Technology, Hanoi University of Industry, No.298, Cau Dien Street, Bac Tu Liem District, Hanoi, Vietnam.
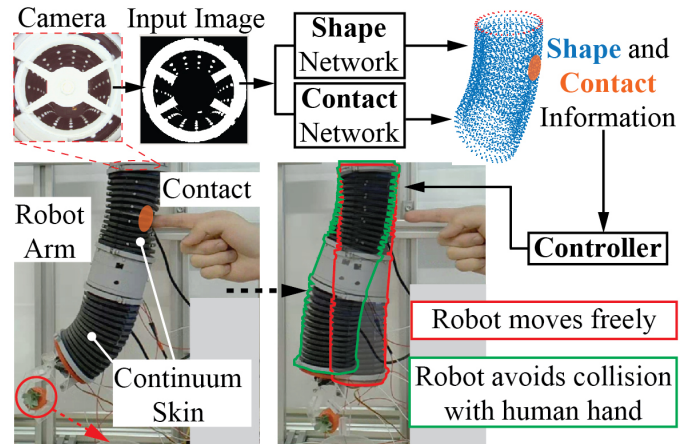* Corresponding author. Email: van-ho@jaist.ac.jp

Fig. 1. Concept of ConTac sensing system. The robot arm state is decided through the shape of the continuum skin, while contact detection allows for contact-aware control.

Analytical calculations provide straightforward solutions for kinematic and dynamic problems of continuum robots [7]–[10] with the cost of having to rely on complex modeling. Another approach to directly perceive the robot's posture is the use of flexible sensors which are integrated into continuum robots in several configurations, such as being attached to [11], [12], or running through the manipulator's body [13]–[15]. However, they require multiple low-resolution sensing units, which could lead to cumbersome device arrangements. Employing a single sensing module at one end of a continuum robot or actuator is another reasonable solution [16], [17] that effectively avoids the potential restriction of the sensing device on the main body. However, the previous studies mostly focus on estimating the robot's posture while contact detection has not been included. Difficulties emerge in realizing a perception mechanism that accurately describes continuum bodies and simultaneously provides the sense of touch. Solving such an issue would greatly enhance the control strategies of continuum robots that aim toward safe robot-environment interaction.

In this paper, we develop the *ConTac* system that can estimate the shape and contact of a continuum-emulated robot with soft skin (see Figure 1). Although the ultimate goal is to implement the proposed platform on a continuum robot, this current work focuses on developing the perception aspect, and an articulated robot arm with a covered soft skin is used as a subject for validation purposes. The system consists of (1)

a backbone that can perform bending movement similar to a continuum robot, (2) a soft skin with markers; (3) a camera observing the skin deformation, (4) models for proprioceptive and tactile sensing of the skin, and (5) contact-aware control regime. We assembled a continuum-emulated robot arm with a backbone and soft skin called the ConTac Unit. The sensing models proposed in this paper for one unit can also be applied for another unit with the same structure and morphology without further calibration. We also present an admittance-based controller that uses the perception information to determine the manipulator's movement. The main contributions of this research can be summarized as:

1) Development of a unified vision-based multimodal sensing platform including two deep-learning models for shape reconstruction and contact detection of the soft continuum skin. The models are trained entirely using simulation images and transferred directly to the domain of real images without fine-tuning.

2) Evaluation of the transferability of the sensing model to other fabricated *ConTac* units without further justification, reducing the development time.

3) Development of a contact-aware control paradigm driven by the *ConTac* sensing information, including the robot's position, velocity, and acceleration, as well as external contact location.

4) Open sourcing the design of the system, allowing for the application for other soft skin and continuum robots.

In Section II, we provide information on the related works. Section III then describes the framework of ConTac for shape and tactile sensing. We then present the evaluation of the system in Section IV, while Section V shows applications and demonstrations. Afterward, we discuss the limitations and future developments of the research in Section VI. Finally, we conclude our work in Section VII.

II. RELATED WORKS

A. Learning-based Shape Sensing for Continuum Bodies

Recently, learning-based sensing techniques have emerged as a reliable model-free approach to estimating the posture of continuum robots. Using capacitive sensors [12], [17], [18] or cameras [16], [19], these techniques can acquire whole-body observation of the deformable structures. Combined with neural networks, such information can be used to reconstruct 3D representation of a highly non-linear body. However, collecting a large quantity of experimental data on such complex morphologies brings challenges in apparatus setup and long-term reliability. Therefore, current data-driven methods for soft body perception utilize simulation platforms to generate and collect artificial data [20]–[23]. Nonetheless, before this knowledge can then be transferred to real-world systems, techniques for minimizing the sim-to-real gap are necessary. Yoo *et al.* [24] reported a sim-to-real pipeline to realize 3D shape sensing model from a single camera captured image for a pneumatic soft robot. To close the sim-to-real gap, they performed calibration of the simulation scene using a real reference image. However, the previous works have the following disadvantages. Firstly, interactions with the surroundings were detected indirectly through the robot's state [18], which could lead to incorrect representations of contact in terms of location and magnitude. Secondly, extensive calibrations using real-world materials are needed [24], which presents difficulties in generalizing such sensing models to other sensors. These problems are addressed in this work.

B. Skin-based Contact Sensing for Robotic Manipulator

In the case that the designs of robots have been predetermined, they can be equipped with skin-type sensors to gain contact awareness while retaining manipulative functions. Electronic sensing skin can be customized to suit a specific scenario. Smaller scaled systems aim toward grasping application [25], [26] or shape recognizing [27], while large-scale ones improve the safety of human-robot interaction [28]. However, the mentioned designs require multiple electronic components, which potentially leads to difficulties in fabrication and calibration. Soft skin combined with vision-based tactile sensing can minimize the mentioned disadvantages since a small number of cameras is utilized to observe large skin areas. Additionally, this method is highly customized and adaptable to different robotic structures [29]–[33]. Luu *et al.* [34] proposed a pipeline for simulation and learning of vision-based tactile sensing that also effectively close the sim-to-real gap. However, in such studies, the tactile skins were fixed onto the rigid robot parts, which were a straight robotic body [30], [31] or a fingertip [32], [33], without actual bending. Additionally, these sensing modules were designed with the consideration of maintaining clear visibility of the internal markers. The mentioned features put restrictions on the ability to adapt such systems to continuum robots. Here, we plan to harness the vision-based multimodal sensing for deformable continuum robot, focusing on solving the marker occlusion caused by the presence of a continuum robot inside the tactile skin.

III. FRAMEWORK FOR SHAPE AND TACTILE SENSING

A. Hardware Design of ConTac System

1) Continuum Tactile Skin: This section proposes the design for a soft skin that can comply with the bending of a multi-joint robot with continuum skin. This bendable property is achieved by the bellows shape with rows of folds which is inspired by morphologies of soft and continuum robots [9], [35] (see Figure 2a). White markers, whose movements can later be monitored by the camera, adhere to the inside of the black deformable skin which blocks most of the ambient light. To realize the proposed skin structure, the molding technique was utilized as described in Figure 2b. The chosen material for the skin and markers was Dragon Skin 10 silicone (Smooth-On, Inc., USA).

2) ConTac Unit: The continuum skin covers an articulated robot arm with two DOF for emulating continuum bending on a plane, while a fish-eye camera (ELP-USBFHD06H-L-180 USB Camera, 30 fps) is placed in a cage-like box and positioned on top of the arm to observe the internal of the
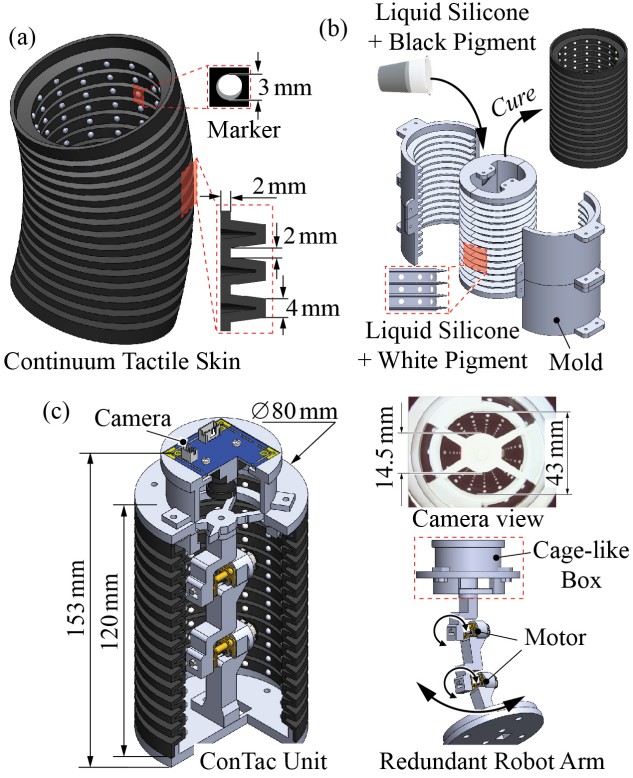
Fig. 2. Hardware design. (a) Continuum tactile skin is bendable and has markers on the inside. (b) Molding method is used to fabricate the soft skin. (c) ConTac Unit consisting of a continuum skin, camera, and a multi-joint robot.

skin (see Figure 3c). LEDs are also attached to the inside of the soft skin to minimize the impact of external lighting conditions and enhance the markers' visibility. The inner arm includes three links, which are 3D printed from PLA plastic, and connected by two DC motors (Pololu, USA). In this study, the two motors receive the same control signal and move simultaneously, therefore, the manipulator is considered as one DOF. The whole module is called the ConTac Unit and weights slightly over 300 grams. We note that the inner arm can be replaced by other types of soft actuators (such as tendon or pneumatic-driven ones).

B. Data Collection

To collect the training data for the shape and contact sensing models, we employed a simulation-based platform to produce simulated images that highly resemble the ones captured by the real camera. As seen in Figure 3, the soft skin is firstly represented as a collection of discrete nodes $\mathbf{X}_0 = [\mathbf{X}_{0,i}, \forall i \in \mathcal{N}] \in \mathbb{R}^{n \times 3}$, each identified by a 3-dimensional vector $\mathbf{X}_{0,i} \in \mathbb{R}^3$. Here, $\mathbf{X}_0$ denotes the initial or undeformed state of the skin, and $i \in \mathcal{N} = \{1, 2, \cdots, n\}$ specifies the index of the node (i.e., $|\mathcal{N}| = n = 4908$). We apply the FEM-based physics engine SOFA [36] to simulate the properties of the soft skin (Young's modulus is 0.1262 MPa and Poisson's ratio is 0.49) and its behavior during operation. Compared to the simulation in [34], where only the soft skin

was considered, we also include a controllable robot arm. For simplification, the motors are replaced by pulling cables. The skin is attached to and complies with the arm, which is similar to the real working condition. Firstly, the multi-joint arm performs bending movements that create an α angle ranging from -40 to 40 degrees with increments of 5 degrees. Here, α is the angle between the perpendicular line with the bottom of the skin and the z-axis. For each bending posture, a pointer pushes into the skin at 80 locations with a depth between 0 to 10 mm with increments of 1 mm. The position vector of a pushed node is $\mathbf{X}_{sim,c}$, while the contact depth is $d_{sim,c} \in \{x \mid x \in \mathbb{Z}, 0 \le x \le 10\}$ with $c \in \mathcal{M}$, where $\mathcal{M}$ is the set of pushed nodes and $|\mathcal{M}| = 80$. As the SOFA model of the skin deforms, the node positions are updated as $\mathbf{X}_{sim,i} \in \mathbb{R}^3$ and used to calculate the node displacement $\mathbf{D}_{sim} = [\mathbf{D}_{sim,i}, \forall i \in \mathcal{N}]$ as follows:

$$\mathbf{D}_{sim,i} = \mathbf{X}_{sim,i} - \mathbf{X}_{0,i} \quad (\forall i \in \mathcal{N}). \tag{1}$$

While SOFA describes the physical characteristics of the system, Unity is utilized to produce realistic images of the skin's deformation. We constructed another skin model in Unity, which receives the displacement data and deforms according to its SOFA counterpart. We note that in the Unity implementation, the components inside the skin are also included, resulting in marker occlusion. This is a feature that would be learned by the models. A virtual wide-angle camera having the same point of view as the real one then captures the skin's deforming. The simulation images (I_{sim}) are the training data for the sensing models, while the simulation node displacement vector ($\mathbf{D}_{sim}$), contact node position ($\mathbf{X}_{sim,c}$), and contact depth ($d_{sim,c}$) are the labels.

C. Shape Sensing and Contact Sensing Model

1) Network Architecture: Figure 4 illustrates the concept of the perception models that utilize two deep learning networks. During training, the simulation images acquired from
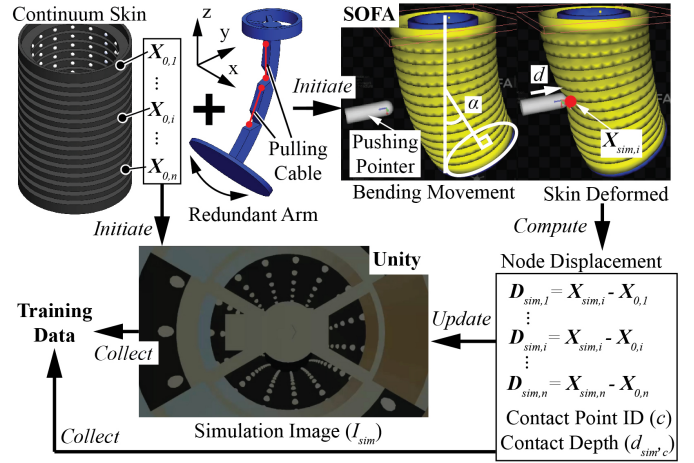

Fig. 3. Data collection process utilizing simulation environment. Both bending movement and external contact are simulated in SOFA. The deformation states of the skin are obtained by SOFA, while the corresponding simulated images are rendered and captured using Unity.

Section III-B are fed into the networks to estimate the desired information, while during inference, the real image is used. Before entering the models, the images are transformed into their binary versions. The Shape Network has the architecture of Unet convolution networks. The output signal includes estimated 3D node displacement vectors $\hat{\mathbf{D}}_i$ of the skin nodes. By combining this shape information with the initial node position $\mathbf{X}_{0,i}$, the position of node i can be identified by vector $\hat{\mathbf{X}}_i \in \mathbb{R}^3$ The skin shape vector can then be reconstructed as:

$$\hat{\mathbf{X}} = [\hat{\mathbf{X}}_1 \, \hat{\mathbf{X}}_2 \, \ldots \, \hat{\mathbf{X}}_n] = \hat{\mathbf{D}} + \hat{\mathbf{X}}_0, \tag{2}$$

where $\hat{\mathbf{D}} = [\hat{\mathbf{D}}_i, \forall i \in \mathcal{N}]$ is the skin displacement vector and $\hat{\mathbf{X}}_0 = [\hat{\mathbf{X}}_{0,i}, \forall i \in \mathcal{N}]$ is the initial skin shape vector. The Contact Network has a similar architecture as the Shape Network, with the exception of the output signal. For this second model, the desired output is the position of the contact location, represented by a three-element vector $\hat{\mathbf{X}}_c$, where c is the index of the pushed point, and the corresponding contact depth $\hat{d}_c$.

2) Network Training and Loss Function: We trained the Shape Network entirely using the simulation dataset obtained from Section III-B. To close the sim-to-real gap, we performed randomization on the training data by using the random affine transformation. We randomly rotated, shifted vertically and horizontally, as well as rescaled the images. The Mean Square Error (MSE) was applied to measure the difference between the predicted node displacement $\hat{\mathbf{D}}_i$ and the ground truth value $\mathbf{D}_{sim,i}$. We define the MSE loss function for the Shape Network as:

$$\mathcal{L}_{shape} = \frac{1}{3n} \sum_{i=1}^{n} \sum_{k \in (x,y,z)} \left(\mathbf{D}_{sim,i}^k - \hat{\mathbf{D}}_i^k \right). \tag{3}$$

For the training of the Contact Network, we proposed a new MSE loss function that measured both the error of contact position and contact depth:

$$\mathcal{L}_{contact} = \frac{1}{3} \sum_{k \in (x,y,z)} \left(\mathbf{X}_{sim,c}^k - \hat{\mathbf{X}}_c^k \right) + \left(d_{sim,c} - \hat{d}_c \right). \tag{4}$$
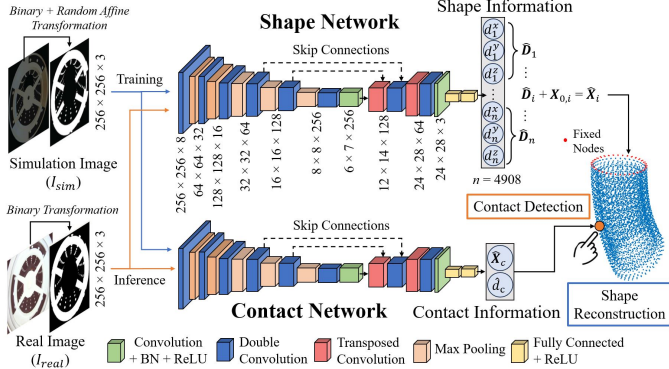

Fig. 4. Architecture of the sensing networks. From a tactile image, the Shape Network predicts the displacement of the skin, while the Contact Network estimates the location and magnitude of the contact. Both models are based on the Unet convolution network.

TABLE I
POSTURES OF CONTAC UNIT IN PROPRIOCEPTIVE EXPERIMENT

Posture No.	0	1	2	3	4
$\alpha_{predict}$ (Degree)	-0.4	6.2	11.2	15.3	20.4

Posture No.	5	6	7	8	9
$\alpha_{predict}$ (Degree)	28.1	31.5	32.7	-5.1	-11.4

Posture No.	10	11	12	13	14
$\alpha_{predict}$ (Degree)	-17.1	-21.8	-26.3	-29.4	-32.9

The chosen optimizer for both networks was stochastic gradient descent (SGD). The learning rate for the Shape Network and Contact Network was 0.0005 and 0.00015, respectively. The training process was done on a desktop computer (Intel Core i7-11700F, GPU: RTX 3060, NVIDIA).

IV. EVALUATION

In this section, we present the experiments conducted to evaluate the performance of the sensing networks. Real data were input into the simulation-data-trained models without additional preprocessing steps.

A. Proprioceptive Sensing

Firstly, we examined the capability of reconstructing the structure of the soft skin from a single image. Figure 5a shows the setup for the shape sensing tests. We attached a ConTac Unit to an overhead base and used a simple PD controller to bend the unit into 14 postures with the corresponding predicted angle α listed in Table I. The predicted α can be derived from the nodal positions $\hat{\mathbf{X}}$ obtained by the Shape Network as follows:

$$\alpha = \frac{\pi}{2} - \cos^{-1} \left(\frac{\hat{\mathbf{X}}_i^z - \hat{\mathbf{X}}_j^z}{\sqrt{(\hat{\mathbf{X}}_i^x - \hat{\mathbf{X}}_j^x)^2 + (\hat{\mathbf{X}}_i^z - \hat{\mathbf{X}}_j^z)^2}} \right), \tag{5}$$

where $(\hat{\mathbf{X}}_i^x, \hat{\mathbf{X}}_i^z)$ and $(\hat{\mathbf{X}}_j^x, \hat{\mathbf{X}}_j^z)$ are the xz coordinates of node $i \in \mathcal{N}$ and $j \in \mathcal{N}$ which together form a line representing the projection of the skin's bottom on the xz-plane. In this case, the two selected nodes are node $i = 1132$ and $j = 240$. We attached 48 reflective markers arranged into 6 evenly spread vertical columns on the outer surface of the skin and placed five OptiTrack cameras surrounding the unit. Using the
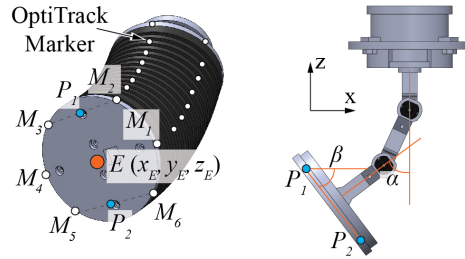

Fig. 5. Experimental setup for shape reconstruction evaluation. (a) Reflective markers are attached to the soft skin and OptiTrack cameras are used to record the real movement of the ConTac Unit. (b) Explanation of reference points on the real device to calculate the evaluation metrics.
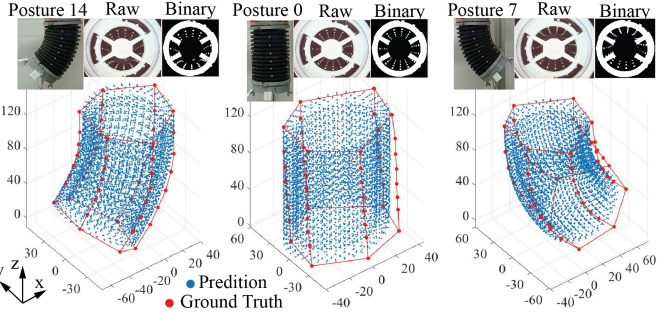
Fig. 6. Samples of shape sensing function. Posture number 0 (neutral state), number 7 ($\alpha > 0$), number 14 ($\alpha < 0$) and their corresponding shape reconstructions and ground-truth shape obtained from OptiTrack.

TABLE II
TIP POSITION ERROR AND ANGLE ERROR OF PROPRIOCEPTIVE EXPERIMENT

	Mean	Standard Deviation
Tip Position Error (mm)	8.8254	2.3346
Angle Error (rad)	0.0920	0.0591

OptiTrack system, the 3D positions of the reflective markers were recorded. Figure 6 shows the shape reconstruction results, illustrated by the point cloud of 4908 points (blue dots), by the Shape Network, and the recorded position of the OptiTrack markers (red dots) for the three postures of number 0, 7, and 14.

The evaluation metrics are the tip position error and angle error. The tip position E can be calculated as the mean of the six reflective markers (from M_1 to M_6) placed on the bottom of the unit, as shown in Figure 5b. The tip position error shows the difference between the predicted location of the unit's end-point and the tip observed by the OptiTrack system. We monitored the bending of the unit through the angle β that is equal to α (described in Section III-B), since the latter could not be directly determined from the outer markers. Here, β is the angle between P_1P_2 and the z-axis, where P_1 is the midpoint of M_2M_3 and P_2 is the midpoint of M_5M_6. We calculated the angle error from the predicted α angle obtained from Equation (5) and the true β angle. Table II shows the results for the two metrics.
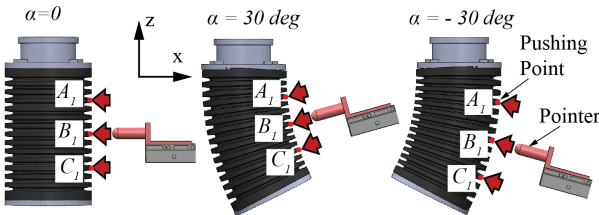

Fig. 7. Experimental setup for contact detection evaluation. (a) A linear stage is used to push into the ConTac unit at predetermined positions. (b) The postures of the unit during the experiment.

TABLE III
POSITIONS OF PUSED POINTS IN CONTACT DETECTION EXPERIMENT

Point	A_1	B_1	C_1	A_2	B_2	C_2
x (mm)	40	40	40	0	0	0
y (mm)	0	0	0	40	40	40
z (mm)	90.88	60	29.12	90.88	60	29.12

Point	A_3	B_3	C_3	A_4	B_4	C_4
x (mm)	-40	-40	-40	0	0	0
y (mm)	0	0	0	-40	-40	-40
z (mm)	90.88	60	29.12	90.88	60	29.12

B. Contact Detection

Figure 7a illustrates the setup for the experiments to evaluate the contact detection function of the system. We identify 12 contact points on the outer side of the soft skin whose positions are shown in Table III. The experimental steps are as follows. The ConTac Unit bends into one of three postures with the according to α angles of (0, $-\pi/6$, $\pi/6$), as seen in Figure 7b. A linear stage pushed into the selected points with various pushing depth values. For each value of depth, the test was repeated three times. We recorded the predictions from the Contact Network and compared them with the true values of pushing depth and location.

Figure 8 reports the prediction of the pushing depth ($d_{predict}$) for the case of contact at the points (A_1, B_1, C_1) and (A_2, B_2, C_2). The former set of contact points represents the scenario where the pushing action is in the same plane as the unit's bending (pushing action is in xz-plane), while the latter set of points represents the case where the pushing action is perpendicular to the bending plane (pushing action is in yz-plane). During in-plane pushing, the predictions agree well with the trend of true values when the contact locations are A_1 and B_1. However, at C_1, significant deviations can be observed. When the pushing motion is perpendicular to the bending plane, the system's predictions successfully capture the trend of the true depth values in all three locations.

We then examined the error between the predicted contact position and its true counterparts in the case of maximum depth pushing. The position error for each pushing point is defined as:

$$error_P = \|(\mathbf{X}_{predict,P} - \mathbf{X}_{true,P}) - \mathbf{d}_{true}\|, \quad (6)$$

where P is one of twelve pushing points, $\mathbf{X}_{predict,P}$ is the predicted 3-D position vector of P, $\mathbf{X}_{true,P}$ is the initial true position vector of P (given in Table III), and $\mathbf{d}_{true}$ is the pushing vector. The results are reported in the form of color maps, in which the error values for other locations on the skin are interpolated from $error_P$ (see Figure 9). The average position error for the pushing points at the upper section of the skin is $\overline{error_{A_i}}$ =16.10 mm ($i = 1, 2, 3, 4$), at the middle section of the skin is $\overline{error_{B_i}}$ =22.34 mm ($i = 1, 2, 3, 4$), and at the lower section of the skin is $\overline{error_{C_i}}$ =46.86 mm ($i = 1, 2, 3, 4$). The average error for the whole skin is 28.86 mm. The results show that the model performs significantly poorer when detecting contact at the
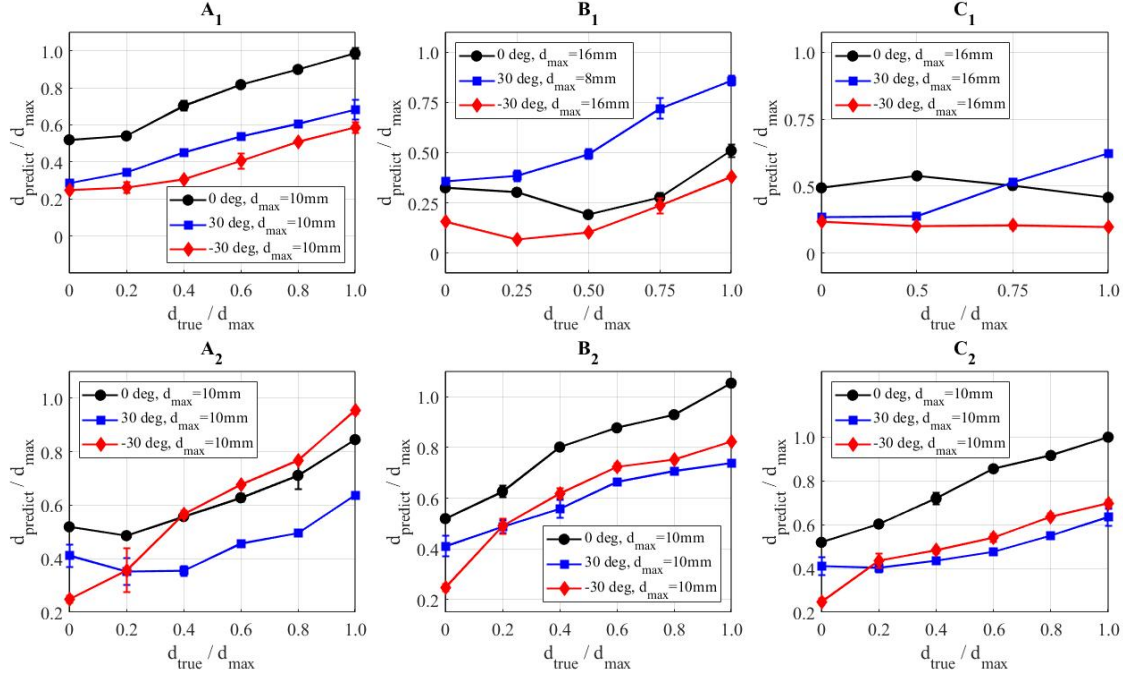
Fig. 8. Comparison between the predicted and real values of pushing depth ($d_{predict}$ and d_{true}). Error bars represent 1 standard deviation. Since the inner multi-joint robot was not completely rigid, when the unit got pushed, there was also slight bending movement. Thus, maximum pushing depth values varied depending on how far that part was from the fixed base (the unit's top).
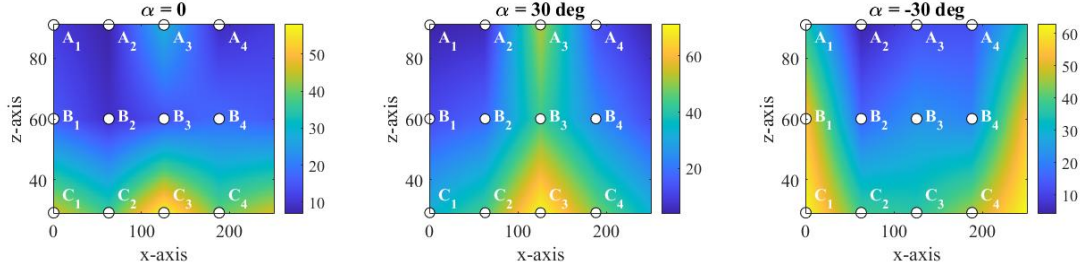

Fig. 9. Color map for error between the predicted and real values of pushing positions. For illustration purposes, the cylindrical skin is unrolled into a surface.

lower part of the skin which is the furthest point from the camera. These points (C_i) are incorrectly predicted to have greater z-coordinates than the true values (see Figure A in Appendix A). These mispredictions, which can be attributed to extreme occlusions at the far end of the camera, greatly raise the average error. However, since the C_i points are located near the base of the skin where contacts might rarely occur, our proposed system remains usable for most contact scenarios in the central region, as demonstrated in Section V. Details of the directional analysis of the contact location error can be found in the Appendix A.

C. Generalizability of Proposed Sim2Real Learning

This section demonstrates the effectiveness of the Shape and Contact Network in generalizing to various instances of ConTac units. A newly assembled ConTac Unit (Unit 2) and the ConTac Unit presented in the previous section (Unit 1)

were used to conduct tests to compare the performance of the sensing model on the two sets of hardware. To evaluate the shape reconstruction function, by using the same control signal for the motors, we bent the two units into three postures shown in Figure 10a and used the Shape Network to estimate the point cloud that represents each unit (see Figure 10b). In all cases, the two cloud points greatly overlap each other, and the average distance error of the two clouds was 0.7436 mm.

To examine the contact detection function, we used the linear stage to push into Unit 1 and Unit 2. The postures (posture a, b, and c), pushing locations (side 1 and side 2), and pushing depth values (10 mm and 16 mm) for the two units were the same (see Figure 11a). The Contact Network then predicts the location and magnitude of the pushing action. The results showed that when the two units had the same posture and the pushing was performed at the same location, the average difference between the two predicted contact
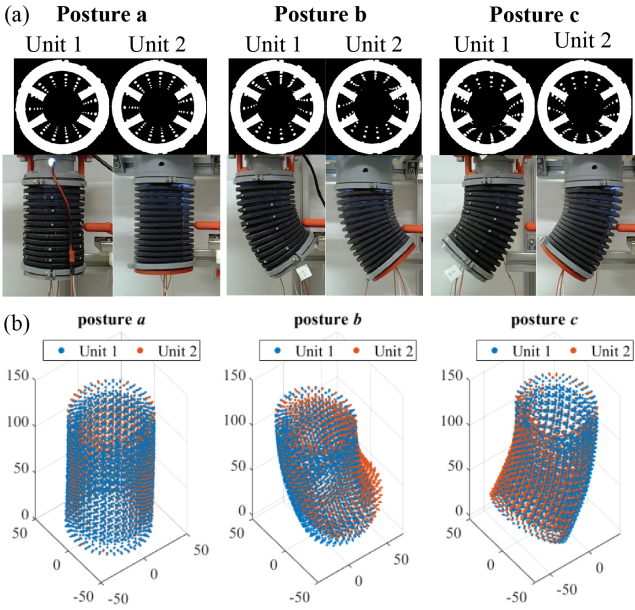
Fig. 10. Shape reconstruction of ConTac Unit 1 and Unit 2. (a) Three postures used in the evaluation and corresponding image input into the Shape Network. (b) Comparison between proprioceptive point clouds of Unit 1 and Unit 2.

points corresponding to the two units was 22.31 mm, while the average difference for contact depth was 2.38 mm. The predicted pushing depths are shown in Figure 11b, although deviations can be observed, the performances of the model on the units agree well, which means that as the pushing depth increased, the predictions corresponding to each unit also increased.
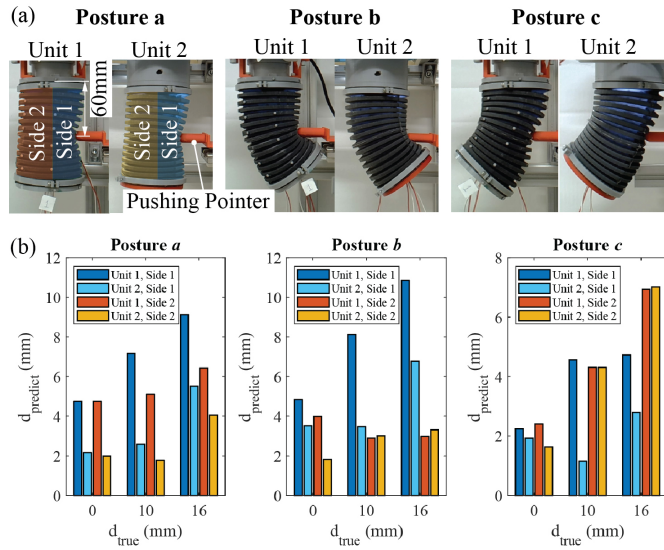

Fig. 11. Contact detection of ConTac Unit 1 and Unit 2. (a) Postures of the two units and positions that the pointer pushes into. (b) Comparison of predicted pushing depth values between Unit 1 and Unit 2.
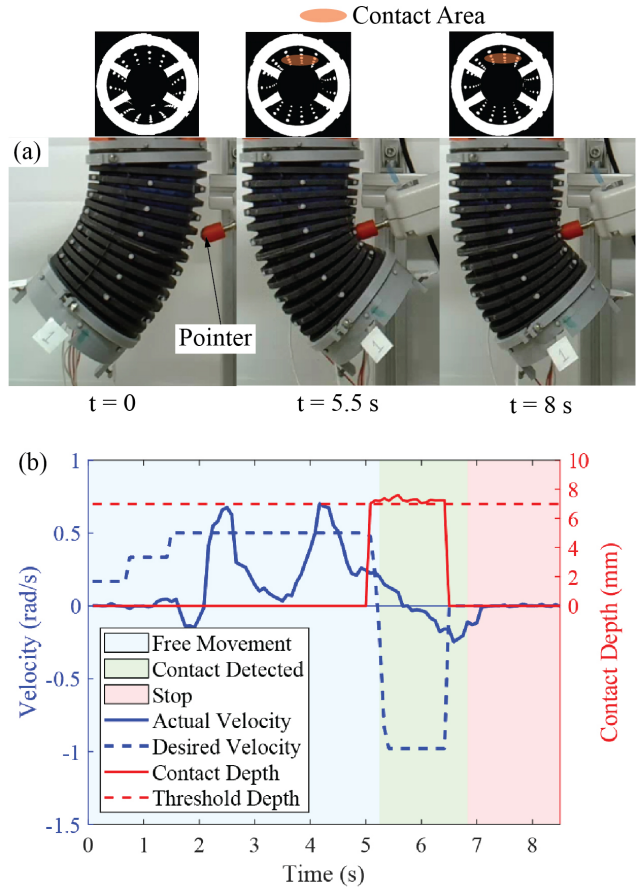

Fig. 12. Sample performance of the ConTac-Driven Control paradigm where $\gamma = 30$ and $c = 1$. (a) Bending movement of the ConTac Unit is obstructed by a pointer. (b) Desired bending velocity, actual bending velocity, and detected contacted depth of the unit.

V. APPLICATIONS

A. Admittance-based Safety Control

This section evaluates the working of the proposed controller in the scenario of the ConTac Unit coming into contact with an object during bending movement.

1) Method: We employ the ConTac-Driven Control paradigm which is an admittance controller [37] utilizing shape and contact information provided by the models. The desired behavior is that the unit moved away from the obstacle until the contact depth fell under a designated threshold d_{th}. The ConTac Unit is treated as a mass-spring-damper system with virtual inertia, damper, and stiffness. The admittance control law for the ConTac Unit with 1 DOF of bending angle α is as follows:

$$\ddot{\alpha}_d = m^{-1} \left(f_c - c\,\dot{\alpha} - k\,\alpha \right), \qquad (7)$$

where $\ddot{\alpha}_d$ is the desired bending acceleration; m is the virtual inertia, c is the virtual damper, and k is the virtual stiffness. We employ a simple elastic model to map the contact force f_c with contact depth:

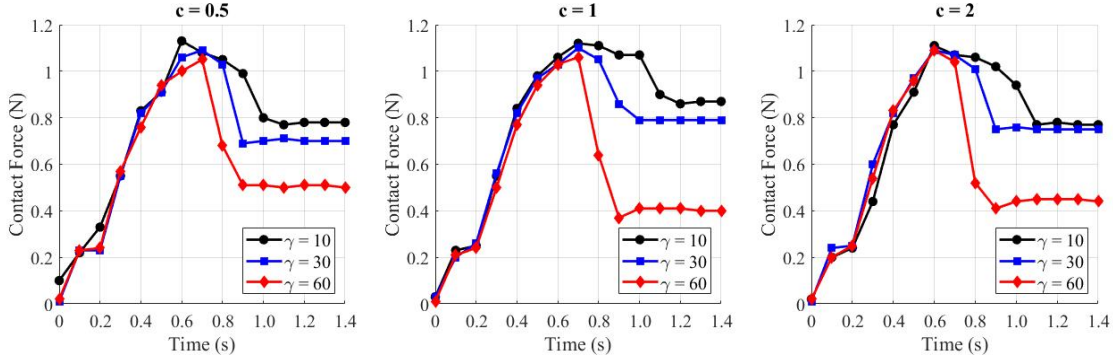$$f_c = \gamma \left(\hat{d}_c - d_{th} \right), \qquad (8)$$

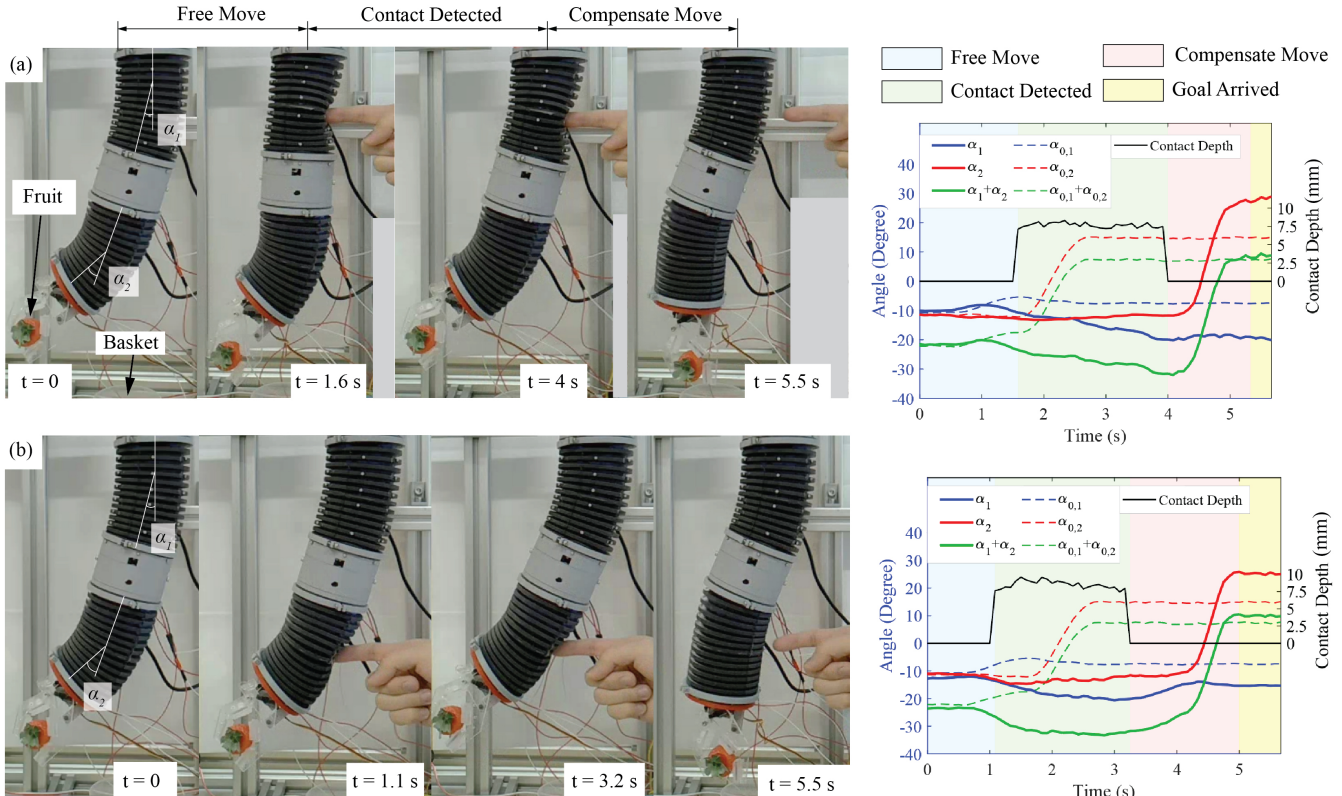Fig. 13. Contact force values correlate with different control parameters.

Fig. 14. Demonstration of redundant robot arm encounter unexpected contact during operation. A human hand pushes into (a) Unit 1 and (b) Unit 2. The graphs show the bending angle values of each unit and the whole arm in obstructed and unobstructed scenarios.

where γ is the elastic constant, $\hat{d}_c$ is the estimated contact depth, and d_{th} is the threshold depth value.

Algorithm 1 describes the operation of the control paradigm. Firstly, the estimated skin deformation vector $\hat{\mathbf{D}}$ and contact depth $\hat{d}_c$ are extracted from the sensing models. The skin shape vector $\hat{\mathbf{X}}$ is then derived using Equation (2). Subsequently, we compute the desired bending acceleration $\ddot{\alpha}_d$, from which the desired bending rate $\dot{\alpha}_d$ can be extrapolated (Alg. 1, lines 9-10). The control signal u is calculated based on an inner loop of PI control to regulate the bending rate $\dot{\alpha}_d$ of *ConTac* unit (see Alg. 1, line 12), which is then converted to the controlled voltage of the motors for driving the *ConTac* motion. The

bending rate feedback $\dot{\alpha}$ is calculated from the estimated bending angle α through the finite difference approximation (Alg. 1, line 7).

2) Performance: The setup for the tests is shown in Figure 12a, where the robot alters its posture from $\alpha = -\pi/6$ to $\alpha = \pi/6$, and a pointer attached to a force gauge (ZTS-20N, IMADA, Japan) serves as an obstacle obstructing the unit's movement. When colliding with the pointer and the contact depth detected by the Contact Network exceeded a threshold of 7 mm, the unit would bend backward and away from the obstacle until the contact depth fell below the threshold. The unit then stopped at an end-posture. In this test, we chose

Algorithm 1 ConTac-Driven Control Algorithm

Input: $\hat{\mathbf{D}}$: skin displacement vector; $\hat{d}_c$: contact depth; d_{th}: contact depth threshold; γ: elastic constant; k: virtual stiffness coefficient; c: virtual damping coefficient; m: virtual mass; α_0: initial bending angle; $\dot{\alpha}_{0,d}$: initial desired velocity; K_p: proportional gain; K_i: integral gain; e_0: initial proportional error; dt: time step

Output: u: motor control signal

1: $\dot{\alpha}_d \leftarrow \dot{\alpha}_{0,d}$
2: $e \leftarrow e_0$
3: $\ddot{\alpha}_{0,d} \leftarrow 0$
4: **while** $\hat{d}_c \geq d_{th}$ **do**
5:    $\hat{\mathbf{X}} \leftarrow calculateSkinShapeVector(\hat{\mathbf{D}})$ ▷ calculate skin shape vector (see Eq. 2)
6:    $\alpha \leftarrow calculateBendingAngle(\hat{\mathbf{X}})$ ▷ calculate bending angle (see Eq. 5)
7:    $\dot{\alpha} \leftarrow (\alpha - \alpha_0)/dt$ ▷ update current bending velocity
8:    $f_c \leftarrow -(\hat{d}_c - d_{th}) \times \gamma$ ▷ convert contact depth to force value (see Eq. 8)
9:    $\ddot{\alpha}_d \leftarrow (f_c - c \times \dot{\alpha} - k \times \alpha)/m$ ▷ calculate desired bending acceleration (see Eq. 7)
10:    $\dot{\alpha}_d \leftarrow \dot{\alpha}_d + dt/2 \times (\ddot{\alpha}_{0,d} + \ddot{\alpha}_d)$
11:    $e \leftarrow e + dt \times (\dot{\alpha}_d - \dot{\alpha})$
12:    $u \leftarrow K_p \times (\dot{\alpha}_d - \dot{\alpha}) + K_i \times e$ ▷ calculate control signal using PI control
13:    $\alpha_0 \leftarrow \alpha$
14:    $\ddot{\alpha}_{0,d} \leftarrow \ddot{\alpha}_d$
15: **end while**

$m = 1$ and $k = 0$. Figure 12b shows the observation of the desired bending angular velocity and the depth detection of the unit in the case of control parameters of $\gamma = 30$ and $c = 1$. We then examined the effect of changing γ and c on the magnitude of contact force recorded by the force gauge. As seen in Figure 13, as γ increased, the final values of contact force decreased. This means that with greater γ, the unit moved backward with greater magnitude to avoid the collision. Additionally, the time required to perform the avoidance was also shortened, meaning the unit moved faster. In contrast, altering c did not noticeably affect the performance of the system.

B. Contact-aware Manipulation

This section demonstrates a pick-and-place application using the ConTac system. We assembled a ConTac Arm by attaching Unit 2, which had a gripper, to the bottom of Unit 1. The arm grasped an object (plastic strawberry) using the gripper from an initial location and dropped the item into a basket at a designated position (see Figure 14a). During the process, a human would unexpectedly touch one of two units and obstruct the movement of the arm. As the contact depth reached a threshold of 7 s, Unit 1 would move away from the human hand to avoid collision. We recorded the bending angle of Unit 1 (α_1) and Unit 2 (α_2) and compared them with the angle values ($\alpha_{0,1}$ and $\alpha_{0,2}$) obtained in the scenario where no contact was present. Figure 14a shows the results of the
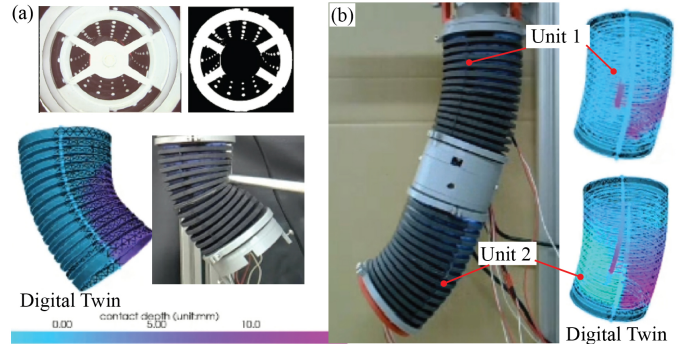

Fig. 15. Visulization of continuum skin via digital twin. (a) Single ConTac Unit. (b) ConTac Arm.

bending angles when the contact is on Unit 1. At around 1.6 s, as the contact depth exceeds 7 mm, the bending angle of Unit 1 quickly decreases, meaning the arm is moving away from the human finger. Unit 1 is now not able to bend into the same posture as when there is no obstruction, which is represented by the deviation between $\alpha_{0,1}$ (blue dashed line) and α_1 (blue line). To compensate for the immobility of Unit 1, Unit 2 performs a greater bending movement indicated by the rapid rise of α_2 (red line). Nevertheless, the sum of α_1 and α_2 (green line), which denotes the movement of the whole arm reaches a similar value as the sum of $\alpha_{0,1}$ and $\alpha_{0,2}$ (green dashed line). This means that the ConTac Arm successfully arrived at the designated location and delivered the object. Figure 14b reports the results for the case where the contact is on Unit 2. A similar collision avoidance strategy was employed and the arm also completed the pick-and-place task.

C. Digital Twin for Continuum Skin

This section shows the application of a digital twin for the continuum skin by using the PyVista library of Python (see Figure 15). The system utilizes the skin shape vector $\hat{\mathbf{X}}$ to reconstruct the shape of the soft skin in real time. Furthermore, the direction and magnitude of the deformation are described through a color map based on the skin displacement vector $\hat{\mathbf{D}}$. The virtual representations provide an intuitive way to observe the behavior of the robot arm through the visualization of the skin, especially in cluttered environments where external visual sensors can not be deployed. Illustration video can be found on our website.

D. Bending Angle Estimation for Soft Backbone

We illustrate the potential of utilizing the ConTac sensing system for a soft structure (see Figure 16). We assembled a completely soft ConTac Unit by replacing the redundant robot arm with a silicone backbone. The unit could perform bending movement by pulling three tendons running along the backbone. The Shape Network was immediately applied for this new unit and retained its functionality in estimating the robot's bending angle, which shows the system's robustness and adaptability. This application proves that the system can be rapidly utilized for shape estimation of a new robot design.
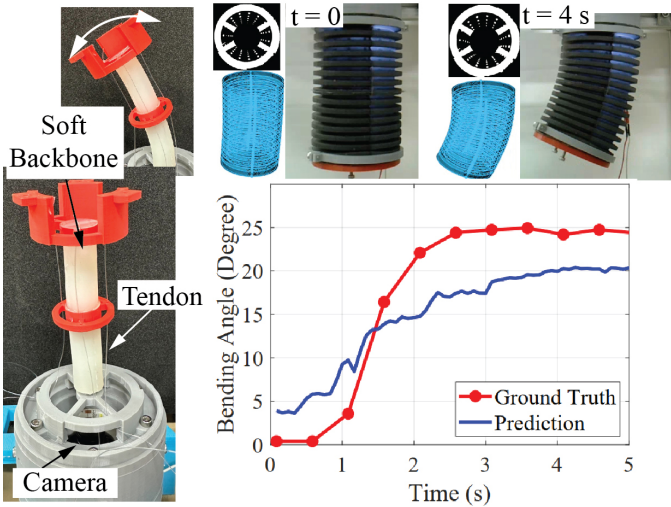
Fig. 16.   ConTac Unit with a soft backbone. We replace the redundant robot arm with a soft backbone that can be bent by pulling tendons. The Shape Network is used to estimate the bending angle of the new unit. The prediction (blue) is compared with the ground truth (red).

VI. DISCUSSION

A. Design of ConTac Unit and Sensing Models

Although the ConTac Unit met the requirements for evaluating the sensing models, some disadvantages need to be addressed. Firstly, in this paper, our inner multi-joint robot arm is limited to planar bending because adding more degrees of freedom (DOFs) would necessitate additional motors, which would increase the load on the base motor. Therefore, a more scalable actuating mechanism is required. Moreover, with a more reliable continuum arm, it is anticipated that analyses involving load handling and realistic object manipulation will be possible. Despite this limitation, the designed continuum skin is cylindrical and radially symmetric, suggesting its potential for integration into 3D movement systems. Secondly, the sensing module consisting of the continuum skin and camera was quite heavy for the redundant robot arms, especially when a second unit was attached. Thus, the workspace of the ConTac Arm was limited. This drawback was mostly due to the size of the chosen camera. In the coming versions, a more compact vision sensor is desirable.

In terms of the designs of the sensing models, although the two networks have similar architecture, we decided to separate them into separate models. In the current stage, this detachment allows for convenience in hyperparameter tuning.

B. Performance of Sensing and Control System

Our system successfully performed the proprioceptive and tactile sensing functions. Based on the training data, the theoretical range of the shape sensing for one ConTac Unit is between -40 deg and 40 deg, while the upper limit depth for the contact prediction is 10 mm. Regarding the drawbacks, the models still possess some restrictions. Firstly, when the contact depth is shallow, the model produces inaccurate predictions (refer to Figure 8). To address this, we established

a threshold to eliminate erroneous estimations. This threshold represents the system's lower detection limit, which is set at 7 mm for the control paradigm discussed in Section V, with respect to 80 mm in diameter of the skin. Despite the limited sensing range in this application, it was adequate for collision avoidance, and extending the contact sensitivity will be our future target.

Concerning the prediction accuracy, as seen in Figure 8, the contact depth predictions for point C_1 largely deviate from the ground truth values. The reason is that compared to A_1 and B_1, C_1 is the furthest away from the camera, therefore, as the ConTac Unit bends, the inside part of the skin corresponding to C_1 could not be seen. A similar trend and explanation can be observed for the contact position error (see Figure 9). Firstly, the error at the skin bottom is greater than at the middle and the top. Secondly, the error at the concave side of the bending skin (corresponding to A_3, B_3, C_3 when α = 30 deg or A_1, B_1, C_1 when α = -30 deg) is greater than the convex side (corresponding to A_1, B_1, C_1 when α = 30 deg or A_3, B_3, C_3 when α = -30 deg). A possible solution is to increase the training data correlated to the contact at the more occluded sections. About the experiment for generalizability, although the models' predictions on both units agreed well with each other, noticeable deviations were still visible since there was no fine-tuning. While we want to avoid tailoring the models to the device, simple and rapid calibration techniques can be advantageous.

Regarding the contact-aware control strategy, we were able to determine the robot's state and detect collision using the same sensing module. In the next stages, we aim to exploit the information about contact location to better decide the avoiding movements, multi-contact detection function will also be explored. Furthermore, as the ConTac Unit is designed as an independent module with its own controller, possibilities for multiple configurations assembled from several units will be explored.

C. Potential of ConTac Sensing for Robot Learning

Our sensing models, which can be zero-shot applied for multiple robot modules, show potential to be applied for preexisting redundant or continuum robots. They could present new solutions to the kinematic and dynamic problems of high-DOF manipulators, while providing additional contact detection, thus improving the control strategies. Our system could also serve as an evaluation apparatus for studies on continuum robots. Furthermore, the softness property of the continuum skin is appropriate for safe human-robot interaction applications. Our design is also low-cost (under 100 USD per ConTac Unit) and can be fabricated from conventional materials. In the following stages, we aim to better generalize the sensing system. Furthermore, different skin morphology will be examined to realize scalable and plug-and-play perception modules.

VII. Conclusion

In this work, we proposed and evaluated the perception system *ConTac* that can estimate the shape and contact of a continuum soft skin. The sensing models were trained entirely using simulation data and could be applied for processing real data from two different ConTac Units without additional calibrations. This generalization was thanks to the simulation environment, which closely resembled the real scenario, and the randomization performed on the training images. We developed an admittance controller utilizing the sensing information and employed it for a robot arm assembled from two ConTac Units. In the future, we aim to address the limitations discussed in Section VI and adapt our sensing models for different types of continuum robots.

References

[1] G. S. Chirikjian and J. W. Burdick, "A hyper-redundant manipulator," *IEEE Robotics & Automation Magazine*, vol. 1, no. 4, pp. 22–29, 1994.

[2] M. W. Hannan and I. D. Walker, "Kinematics and the implementation of an elephant's trunk manipulator and other continuum style robots," *Journal of robotic systems*, vol. 20, no. 2, pp. 45–63, 2003.

[3] B. A. Jones and I. D. Walker, "Kinematics for multisection continuum robots," *IEEE Transactions on Robotics*, vol. 22, no. 1, pp. 43–55, 2006.

[4] J. Burgner-Kahrs, D. C. Rucker, and H. Choset, "Continuum robots for medical applications: A survey," *IEEE Transactions on Robotics*, vol. 31, no. 6, pp. 1261–1280, 2015.

[5] K. Ma, X. Chen, J. Zhang, Z. Xie, J. Wu, and J. Zhang, "Inspired by physical intelligence of an elephant trunk: Biomimetic soft robot with pre-programmable localized stiffness," *IEEE Robotics and Automation Letters*, vol. 8, no. 5, pp. 2898–2905, 2023.

[6] H. Jiang, Z. Wang, Y. Jin, X. Chen, P. Li, Y. Gan, S. Lin, and X. Chen, "Hierarchical control of soft manipulators towards unstructured interactions," *The International Journal of Robotics Research*, vol. 40, no. 1, pp. 411–434, 2021.

[7] D. C. Rucker and R. J. Webster III, "Statics and dynamics of continuum robots with general tendon routing and external loading," *IEEE Transactions on Robotics*, vol. 27, no. 6, pp. 1033–1044, 2011.

[8] W. S. Rone and P. Ben-Tzvi, "Continuum robot dynamics utilizing the principle of virtual power," *IEEE Transactions on Robotics*, vol. 30, no. 1, pp. 275–287, 2013.

[9] V. Falkenhahn, T. Mahl, A. Hildebrandt, R. Neumann, and O. Sawodny, "Dynamic modeling of bellows-actuated continuum robots using the euler–lagrange formalism," *IEEE Transactions on Robotics*, vol. 31, no. 6, pp. 1483–1496, 2015.

[10] K. Oliver-Butler, J. Till, and C. Rucker, "Continuum robot stiffness under external loads and prescribed tendon displacements," *IEEE Transactions on Robotics*, vol. 35, no. 2, pp. 403–419, 2019.

[11] Z. Xie, F. Yuan, Z. Liu, Z. Sun, E. M. Knubben, and L. Wen, "A proprioceptive soft tentacle gripper based on crosswise stretchable sensors," *IEEE/ASME transactions on mechatronics*, vol. 25, no. 4, pp. 1841–1850, 2020.

[12] R. L. Truby, C. Della Santina, and D. Rus, "Distributed proprioception of 3d configuration in soft, sensorized robots via deep learning," *IEEE Robotics and Automation Letters*, vol. 5, no. 2, pp. 3299–3306, 2020.

[13] I. Van Meerbeek, C. De Sa, and R. Shepherd, "Soft optoelectronic sensory foams with proprioception," *Science Robotics*, vol. 3, no. 24, p. eaau2489, 2018.

[14] G. Soter, A. Conn, H. Hauser, and J. Rossiter, "Bodily aware soft robots: integration of proprioceptive and exteroceptive sensors," in *2018 IEEE international conference on robotics and automation (ICRA)*. IEEE, 2018, pp. 2448–2453.

[15] Y. Toshimitsu, K. W. Wong, T. Buchner, and R. Katzschmann, "Sopra: Fabrication & dynamical modeling of a scalable soft continuum robotic arm with integrated proprioceptive sensing," in *2021 IEEE/RSJ International Conference on Intelligent Robots and Systems (IROS)*. IEEE, 2021, pp. 653–660.

[16] M. Hofer, C. Sferrazza, and R. D'Andrea, "A vision-based sensing approach for a spherical soft robotic arm," *Frontiers in Robotics and AI*, vol. 8, p. 630935, 2021.

[17] W. Ouyang, L. He, A. Albini, and P. Maiolino, "A modular soft robotic arm with embedded tactile sensors for proprioception," in *2022 IEEE 5th International Conference on Soft Robotics (RoboSoft)*. IEEE, 2022, pp. 919–924.

[18] L. Scimeca, J. Hughes, P. Maiolino, and F. Iida, "Model-free soft-structure reconstruction for proprioception using tactile arrays," *IEEE Robotics and Automation Letters*, vol. 4, no. 3, pp. 2479–2484, 2019.

[19] Y. She, S. Q. Liu, P. Yu, and E. Adelson, "Exoskeleton-covered soft finger with vision-based proprioception and tactile sensing," in *2020 ieee international conference on robotics and automation (icra)*. IEEE, 2020, pp. 10 075–10 081.

[20] Z. Ding, N. F. Lepora, and E. Johns, "Sim-to-real transfer for optical tactile sensing," in *2020 IEEE International Conference on Robotics and Automation (ICRA)*. IEEE, 2020, pp. 1639–1645.

[21] C. Sferrazza, T. Bi, and R. D'Andrea, "Learning the sense of touch in simulation: a sim-to-real strategy for vision-based tactile sensing. in 2020 ieee," in *RSJ International Conference on Intelligent Robots and Systems (IROS)*, pp. 4389–4396.

[22] S. Wang, M. Lambeta, P.-W. Chou, and R. Calandra, "Tacto: A fast, flexible, and open-source simulator for high-resolution vision-based tactile sensors," *IEEE Robotics and Automation Letters*, vol. 7, no. 2, pp. 3930–3937, 2022.

[23] Z. Si, Z. Zhu, A. Agarwal, S. Anderson, and W. Yuan, "Grasp stability prediction with sim-to-real transfer from tactile sensing," in *2022 IEEE/RSJ International Conference on Intelligent Robots and Systems (IROS)*. IEEE, 2022, pp. 7809–7816.

[24] U. Yoo, H. Zhao, A. Altamirano, W. Yuan, and C. Feng, "Toward zero-shot sim-to-real transfer learning for pneumatic soft robot 3d proprioceptive sensing," *arXiv preprint arXiv:2303.04307*, 2023.

[25] J. Kim, A. Alspach, and K. Yamane, "3d printed soft skin for safe human-robot interaction," in *2015 IEEE/RSJ International Conference on Intelligent Robots and Systems (IROS)*. IEEE, 2015, pp. 2419–2425.

[26] T. P. Tomo, A. Schmitz, W. K. Wong, H. Kristanto, S. Somlor, J. Hwang, L. Jamone, and S. Sugano, "Covering a robot fingertip with uskin: A soft electronic skin with distributed 3-axis force sensitive elements for robot hands," *IEEE Robotics and Automation Letters*, vol. 3, no. 1, pp. 124–131, 2017.

[27] T. P. Tomo, M. Regoli, A. Schmitz, L. Natale, H. Kristanto, S. Somlor, L. Jamone, G. Metta, and S. Sugano, "A new silicone structure for uskin—a soft, distributed, digital 3-axis skin sensor and its integration on the humanoid robot icub," *IEEE Robotics and Automation Letters*, vol. 3, no. 3, pp. 2584–2591, 2018.

[28] Q. Leboutet, E. Dean-Leon, F. Bergner, and G. Cheng, "Tactile-based whole-body compliance with force propagation for mobile manipulators," *IEEE Transactions on Robotics*, vol. 35, no. 2, pp. 330–342, 2019.

[29] D. F. Gomes, P. Paoletti, and S. Luo, "Generation of gelsight tactile images for sim2real learning," *IEEE Robotics and Automation Letters*, vol. 6, no. 2, pp. 4177–4184, 2021.

[30] B. Ward-Cherrier, N. Pestell, L. Cramphorn, B. Winstone, M. E. Giannaccini, J. Rossiter, and N. F. Lepora, "The tactip family: Soft optical tactile sensors with 3d-printed biomimetic morphologies," *Soft robotics*, vol. 5, no. 2, pp. 216–227, 2018.

[31] N. M. D. Le, N. H. Nguyen, D. A. Nguyen, T. D. Ngo, and V. A. Ho, "Viart: Vision-based soft tactile sensing for autonomous robotic vehicles," *IEEE/ASME Transactions on Mechatronics*, vol. 29, no. 2, pp. 1420–1430, 2024.

[32] H. Sun, K. J. Kuchenbecker, and G. Martius, "A soft thumb-sized vision-based sensor with accurate all-round force perception," *Nature Machine Intelligence*, vol. 4, no. 2, pp. 135–145, 2022.

[33] I. Andrussow, H. Sun, K. J. Kuchenbecker, and G. Martius, "Minsight: A fingertip-sized vision-based tactile sensor for robotic manipulation," *Advanced Intelligent Systems*, vol. 5, no. 8, p. 2300042, 2023.

[34] Q. K. Luu, N. H. Nguyen, and V. A. Ho, "Simulation, learning, and application of vision-based tactile sensing at large scale," *IEEE Transactions on Robotics*, vol. 39, no. 3, pp. 2003–2019, 2023.

[35] J. A. Childs and C. Rucker, "Concentric precurved bellows: New bending actuators for soft robots," *IEEE Robotics and Automation Letters*, vol. 5, no. 2, pp. 1215–1222, 2020.

[36] F. Faure, C. Duriez, H. Delingette, J. Allard, B. Gilles, S. Marchesseau, H. Talbot, H. Courtecuisse, G. Bousquet, I. Peterlik *et al.*, "Sofa: A multi-model framework for interactive physical simulation," *Soft tissue biomechanical modeling for computer assisted surgery*, pp. 283–321, 2012.

[37] S. Haddadin, A. Albu-Schaffer, A. De Luca, and G. Hirzinger, "Collision detection and reaction: A contribution to safe physical human-robot interaction," in *2008 IEEE/RSJ International Conference on Intelligent Robots and Systems*. IEEE, 2008, pp. 3356–3363.

[38] S. Sareh, Y. Noh, M. Li, T. Ranzani, H. Liu, and K. Althoefer, "Macrobend optical sensing for pose measurement in soft robot arms," *Smart Materials and Structures*, vol. 24, no. 12, p. 125024, 2015.

[39] F. Monet, S. Sefati, P. Lorre, A. Poiffaut, S. Kadoury, M. Armand, I. Iordachita, and R. Kashyap, "High-resolution optical fiber shape sensing of continuum robots: A comparative study," in *2020 IEEE international conference on robotics and automation (ICRA)*. IEEE, 2020, pp. 8877–8883.

APPENDIX

A. ANALYSIS OF CONTACT ERROR

To evaluate the magnitude and direction of the positional contact error, the following analysis is conducted. For ease of error comparison relative to the full scale of the skin, the soft skin is unrolled onto the uz plane, aligning the u and z axes with the circumference and height of the soft skin. The localization error of a prediction is defined as the vector $\mathbf{v}_P$ that points from the true pushing point to its predicted counterpart:

$$\mathbf{v}_P = (u_P, z_P),$$

$$u_P = s\sqrt{\left(\mathbf{X}_{predict,P}^x - \mathbf{X}_{true,P}^x\right)^2 + \left(\mathbf{X}_{predict,P}^y - \mathbf{X}_{true,P}^y\right)^2},$$

$$z_P = \mathbf{X}_{predict,P}^z - \mathbf{X}_{true,P}^z,$$

$$s = sign\left(A\right),$$

$$A = \arctan\left(\mathbf{X}_{predict,P}^x - \mathbf{X}_{true,P}^x, \mathbf{X}_{predict,P}^y - \mathbf{X}_{true,P}^y\right).$$

where $(\mathbf{X}_{true,P}^x, \mathbf{X}_{true,P}^y, \mathbf{X}_{true,P}^z)$ are the xyz coordinates of true pushing point, while $(\mathbf{X}_{predict,P}^x, \mathbf{X}_{predict,P}^y, \mathbf{X}_{predict,P}^z)$ are the xyz coordinates of predicted pushing point.

The results for the relative and absolute localization errors are reported in Table IV and Figure A, respectively. In this analysis, the result is the average of the values from the three cases corresponding to three bending angles (0, 30, and -30 degrees). At the bottom section of the skin (points C_i), the system gives significantly poorer predictions. Developing advanced processing algorithms, such as occlusion removal learning, to reduce significant prediction gaps in the extreme
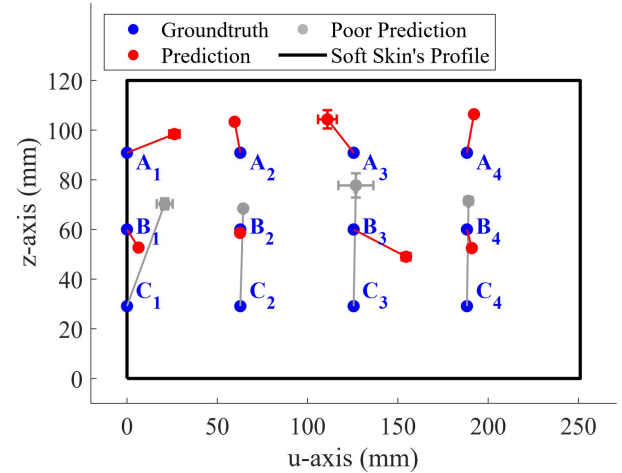

Fig. 17. Illustration for the contact localization errors in comparison with the soft skin's scale.

TABLE V
TIP POSITION AND ANGLE ERROR OF PROPRIOCEPTION FOR REDUNDANT ROBOTS

Ref	Sensing Method	Robot's Length (mm)	Tip Error (mm)	Angle Error (rad)
[38]	Optical Fiber	40	N/A	0.244
[39]	Optical Fiber	35	0.32	N/A
[16]	Vision-based	N/A	N/A	0.018
[24]	Vision-based	100	10.12	N/A
This work	Vision-based	120	8.83	0.092

and most occluded regions is one of our objectives for future work.

B. QUANTITATIVE ANALYSIS OF TIP POSITION ERROR

Table V provides a comparison between the performance of the shape-sensing methods for soft and redundant robots. The selected robots have similar body morphology. Our work is comparable to previous studies while also integrating contact detection function, which was not present in the early works.

TABLE IV
QUANTITATIVE RESULTS FOR CONTACT LOCALIZATION ERRORS. THE ERRORS ARE MEASURED IN SCALE WITH THE SOFT SKIN'S SIZE, IN RELATION TO THE SKIN'S CIRCUMFERENCE AND HEIGHT, $u_p' = u_p/C \times 100\%$; $z_p' = z_p/H \times 100\%$; $C = 251\,mm$; $H = 120\,mm$

P	i = 1		i = 2	
	u_P'	z_P'	u_P'	z_P'
A_i	10.47 ± 0.47	6.28 ± 0.96	-1.254 ± 1.15	10.39 ± 0.63
B_i	2.55 ± 0.17	-6.07 ± 0.39	-0.06 ± 0.51	-1.14 ± 0.24
C_i	8.32 ± 1.75	34.32 ± 1.84	0.65 ± 0.30	32.77 ± 0.29

P	i = 3		i = 4	
	u_P'	z_P'	u_P'	z_P'
A_i	-5.78 ± 2.06	11.22 ± 3.07	1.55 ± 0.43	12.92 ± 0.22
B_i	11.57 ± 0.98	-9.15 ± 1.06	1.08 ± 0.42	-6.25 ± 0.63
C_i	0.50 ± 3.86	40.51 ± 4.06	0.35 ± 0.89	35.34 ± 1.26